

## **EFFECTS OF POST-TENSIONING AND ENERGY DISSIPATORS ON SEISMIC PERFORMANCE OF BRIDGE**

Alex Piolatto  
Southern Illinois University at Carbondale  
University of Nevada, Reno  
Dr. David Sanders  
Kevin Almer

### **Abstract**

An analytical study was performed using the SAP2000 finite element analysis software. Static and seismic loads were applied to four different bridge systems in the longitudinal direction. Variables of interest were post-tensioning in the column pier and placement of lead rubber bearings at the abutments. A static push-over analysis demonstrated that the system with the unbonded post-tensioned column had a 4.95in smaller displacement capacity than the system with the conventionally reinforced column. Dynamic analysis showed that the system with the unbonded post-tensioned column experienced greater peak displacements than the system with the conventionally reinforced column. Residual displacements for the system with the unbonded post-tensioned column were an average of 1.40in smaller. Adding lead rubber bearings to the system with the unbonded post-tensioned column reduced peak displacements by an average of 1.25in.

## Introduction

In seismic areas, bridges are designed so that the columns will yield rather than the superstructure. Ductile columns dissipate energy that otherwise damages the rest of the bridge. Many such columns are reinforced with bonded steel. While this design allows for energy dissipation, it has a weakness. Powerful earthquakes cause residual displacement of the column. This permanent deformation can be difficult to repair. Unbonded post-tensioning solves the problem of residual displacement. Since strain is distributed equally throughout the tendon, it does not yield easily, and residual displacements are small (Kwan and Billington, 2003). However, less yielding in the tendons results in lower energy dissipation. Previous studies investigated the effects of combining bonded longitudinal reinforcement with unbonded post-tensioning reinforcement.

Kwan and Billington performed monotonic, cyclic, and dynamic analyses on a single column pier and a two-column bent using both single degree of freedom and finite element analysis models. They used four systems: one with unbonded post-tensioning only; one with unbonded post-tensioning and some mild reinforcement; one with mild reinforcement and some unbonded post-tensioning; and one with mild reinforcement only. Their push-over analyses showed that systems with a higher degree of unbonded pre-stressing have lower ultimate displacement capacities. It was also demonstrated that systems with lower energy dissipation experience greater peak displacements, and the system that had the largest peak displacements was the system with unbonded post-tensioning. In addition, they defined criteria for functional and survival-level performance and found that systems with an optimal combination of mild reinforcement and unbonded post-tensioning have the best functional-level performance while systems with mild reinforcement have the best survival-level performance.

Mahin et. al. proposed replacing some longitudinal reinforcing bars with an unbonded post-tensioning tendon in order to reduce residual displacements. Through shake table testing and computer analysis, they found that placing an unbonded pre-stressing strand in the center of a lightly reinforced concrete column reduces residual displacements to ten percent of conventionally detailed columns. Peak responses were found to be nearly identical for both designs. They also found that unbonding some of the mild reinforcing bars enhances the self-centering capability. It is worth noting that their computer analyses predicted 90% smaller residual displacement for the conventionally detailed column and 100% larger residual displacement for the column with the unbonded pre-stressing strand.

These previous studies show that a combination of unbonded post-tensioning and mild steel can increase energy dissipation while reducing residual displacement. There are also other ways to increase energy dissipation. Lead rubber bearings (LRBs) may be placed at the abutments. A study has shown that utilizing LRBs can decrease longitudinal deflections and reduce the shear demand in a column pier (Buckle and Mayes, 1990).

Post-tensioning is particularly well-suited for precast concrete and accelerated construction. Using precast concrete reduces work such as formwork, which allows for shorter construction time (Yamashita and Sanders, 2005). Whereas cast-in-place construction causes traffic problems, precast concrete alleviates many woes of construction in an urban area. Other benefits of accelerated construction are its high quality and low life cycle cost.

The purpose of this study was to examine the static and dynamic responses of four different precast bridge systems. Variables were type of column reinforcement and the presence of LRBs at the abutments. The first system featured a conventionally detailed column, and the

second system featured a column with unbonded post-tensioning strands for the longitudinal reinforcement. The last two systems were identical to the first two except that they featured LRBs at the abutments. All four systems had identical superstructures, and the physical dimensions of the column were also the same.

A computer analysis was performed using the SAP2000 finite element analysis software. Each system underwent a static push-over analysis and four dynamic analyses in the longitudinal direction. Special attention was paid to the maximum and residual displacements.

### Modeling

In the summer of 2007, quasi-static tests were performed on a 40% scale bridge at the University of Nevada, Reno Large Scale Structures Laboratory. The tests were performed by PhD student Kevin Almer and PI David Sanders. The purpose of their study was to develop and examine integral connection details of precast superstructures with cast-in-place bent caps subjected to longitudinal seismic loading (Almer and Sanders, 2006). The template used for analytical modeling in this study was full-scale, and it was based off of their 40% scale model. The bridge had a single column pier and two spans. It was simply supported at the abutments. The superstructure was made up of two precast U-girder segments and an integral connection to the column.

Although Almer and Sanders tested a circular cast-in-place concrete column, a hollow rectangular column was used in this study. It was a copy of a design used by Yamashita and Sanders. In order to obtain desirable steel to concrete ratios, the column had to be scaled down 50% from their prototype. All of the columns used in the systems were designed to have moment capacities of about 74,400kip-in because that was the moment capacity of Almer’s full-scale prototype. Universal system characteristics are shown in Table 1, Fig. 1, and Fig. 2. For a three-dimensional view, see Figure 8 in the appendix. The weak direction of the column was aligned with the longitudinal direction of the bridge. The system with a conventionally detailed column was referred to as RC. The system with an unbonded post-tensioned column was called PT. RCL and PTL were the names of the last two systems, which were identical to the first two but with the addition of LRBs at the abutments.

**Table 1.** Universal system characteristics

Superstructure Span	2,390in
Column Height	289.75in
Column Width	80in
Column Length	36in
Flange/Web Thickness of Column	7.5in
Column Moment Capacity	74,400kip-in

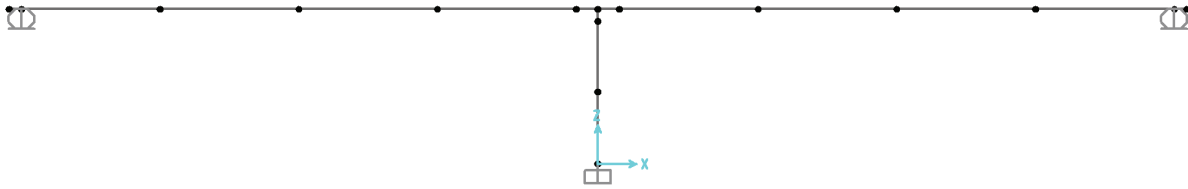


**Figure 1.** Bridge template used for analysis

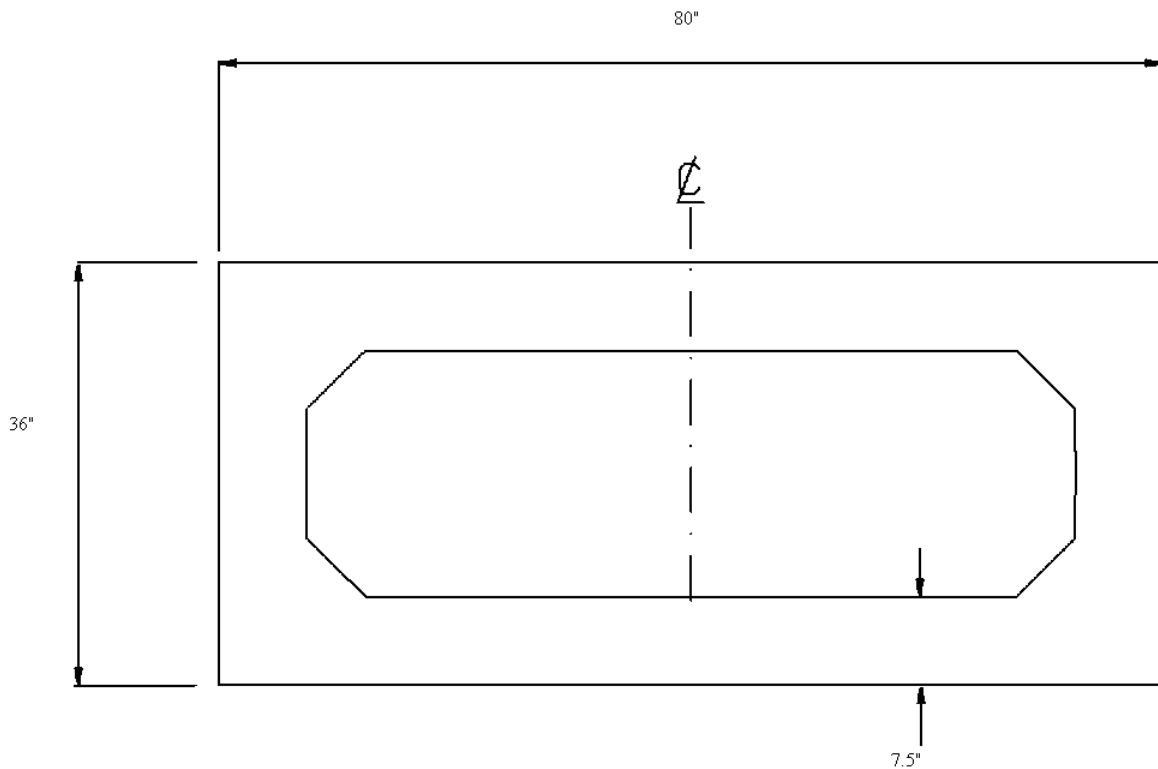


**Figure 2.** Column template used for analysis

All of the nonlinearity was expressed in plastic hinges located at the top and bottom of the column. The plastic hinges were modeled using multi-linear plastic link elements. The links were given a length of 0.1in. The axial and shear forces were modeled as linear, and the moment about the y-axis was modeled as nonlinear with the Takeda hysteresis. In order to define the nonlinear behavior of the plastic hinge, it was necessary to determine the moment-rotation relationship of each system.

*Conventionally Designed Column (RC and RCL)*

Designing the reinforcement was the first step in defining the nonlinear behavior of the column. XTRACT was used (Fig. 3). The target moment capacity of the column was 74,400kip-in, and a moment capacity of 68,920kip-in was achieved. Moment-curvature analysis provided the details that were necessary to establish the moment-rotation relationship, which was simplified to a bi-linear relationship (Fig. 4). The XTRACT analysis also provided information necessary to calculate axial and shear stiffness. Further details regarding the confined concrete model and the moment-rotation relationship can be found in the appendix.

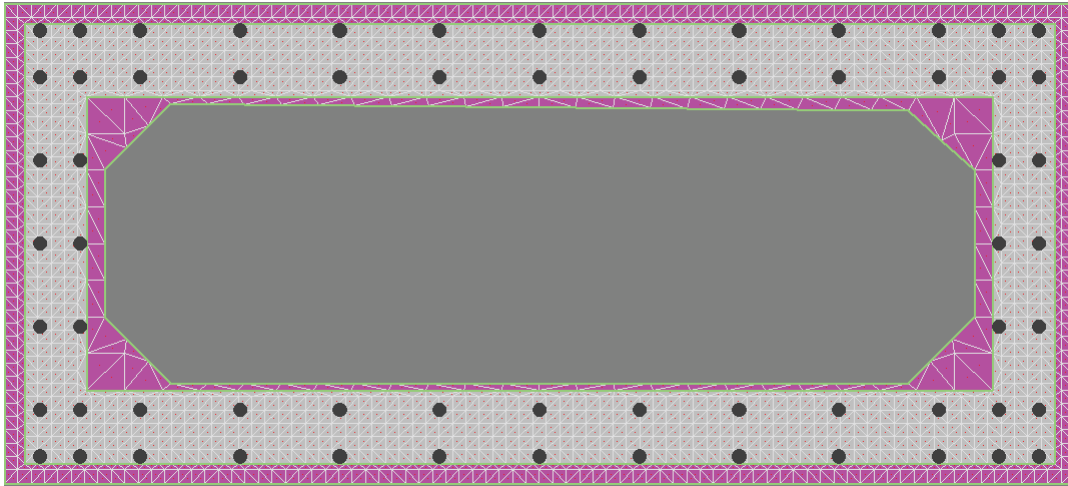


**Figure 3.** XTRACT model

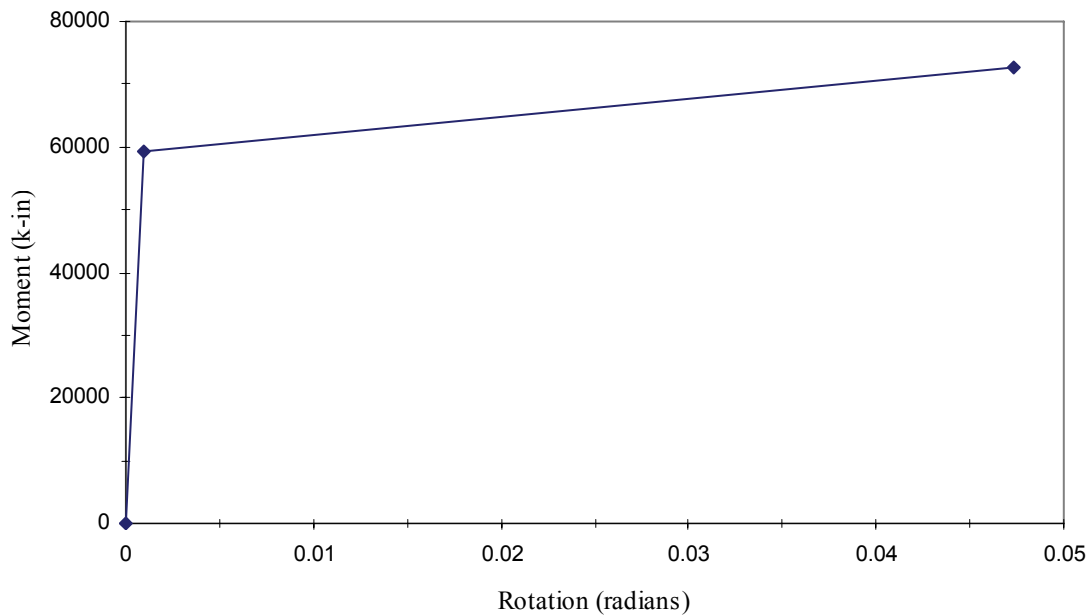


**Figure 4.** Moment-rotation relationship used to define link element of RC

*Unbonded Post-tensioned Column (PT and PTL)*

It was not possible to perform an accurate moment-curvature analysis on the unbonded post-tensioned column because XTRACT is not capable of modeling that form of pre-stressing. Therefore, other options had to be entertained, and ultimately, only one was found. Yamashita used a simplified method to calculate the moment-drift relationship of a hollow rectangular post-tensioned column. His curve was tri-linear. However, his method was applied to a cantilever column. Since the column used in this study was in double curvature, modifications to Yamashita's technique were made.

First, the flexural design of the column had to be performed. It was assumed that shear reinforcement was provided such that crushing of the core concrete did not occur. A cross-section of the post-tensioned column is shown in Fig. 5. The moment-drift relationship was defined in three steps: the theoretical moment and drift at joint opening were found; the relationship between the resultant location of the compressive force and the drift was defined; and the moments upon the compressive force reaching its maximum distance from the centroid, yielding, and failure were found. After determining the moment-drift relationship, the moment-rotation relationship was defined using trigonometry. The moment-rotation relationship is shown in Fig. 6. The axial stiffness for the PT column was the same as the RC column, and the shear stiffness was determined from the moment-rotation relationship. For a more detailed discussion of the above computations, see the appendix.

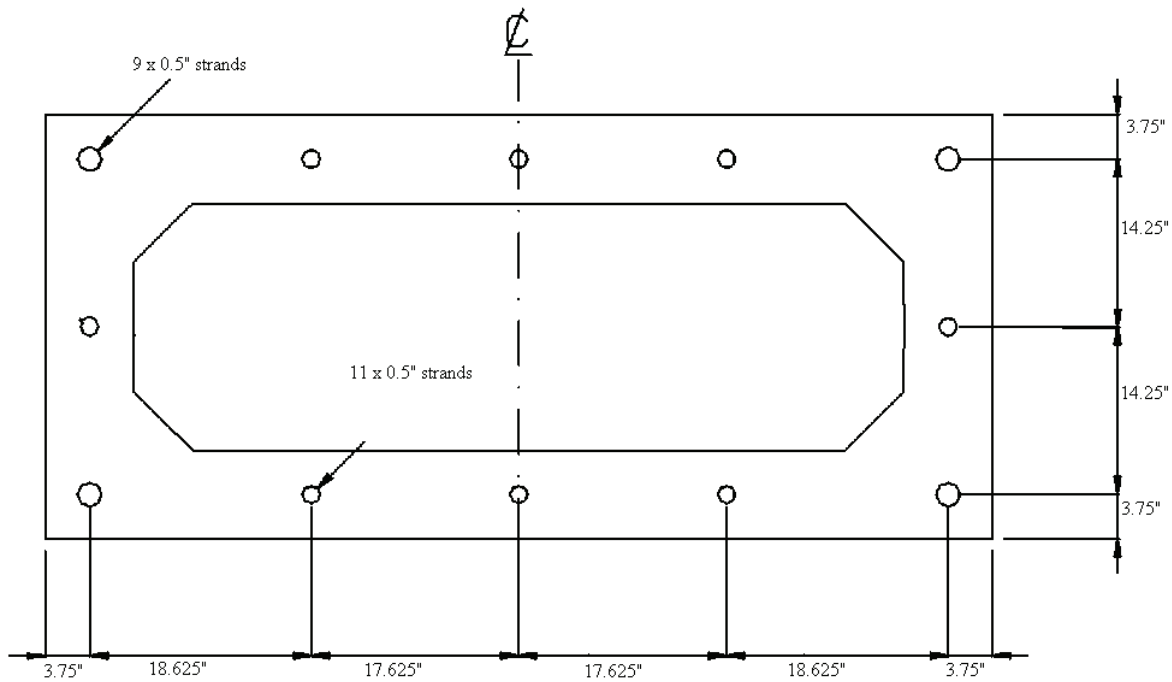


**Figure 5.** Reinforcement details for PT

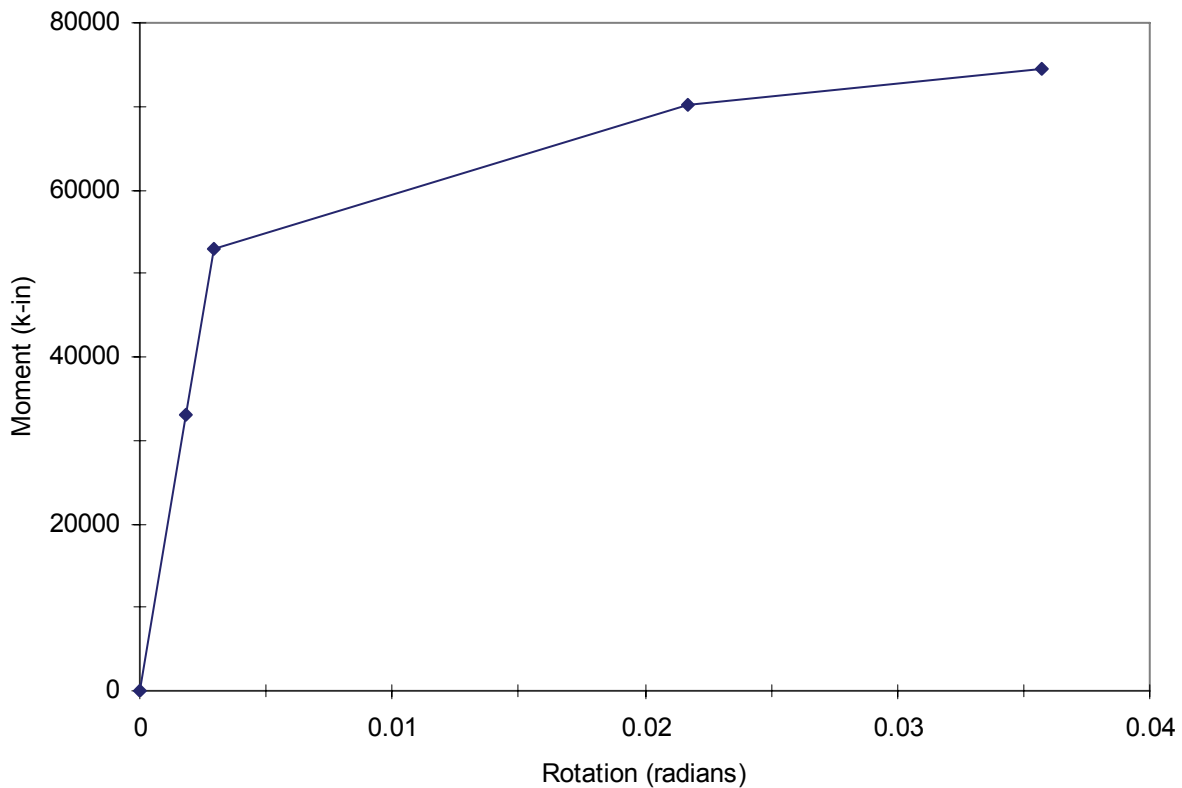


**Figure 6.** Moment-rotation relationship used to define link element of PT

*Dampers*

The lead rubber bearings were modeled as multi-linear plastic link elements, and they were designed from specifications provided by Dynamic Isolation Systems, Inc. of Sparks, NV. The LRBs were only allowed to deform in the longitudinal direction. Details of the design process and characteristics of the dampers are located in the appendix.

*Ground Motions*

All ground acceleration records were obtained from the Pacific Earthquake Engineering Research (PEER) website. They were selected based on the proximity of the recording station to the fault rupture and peak ground acceleration. It was thought that these criteria would result in intense ground motions. The purpose of such selections was to elicit as great a response out of each system as possible without causing a given system to fail. Four earthquakes were selected in total: 1992 Cape Mendocino; 1971 San Fernando; 1983 Coalinga; and 1991 Chi-Chi, Taiwan. The motion used from the 1992 Cape Mendocino quake came from the Cape Mendocino station, which is located 8.5km from the fault rupture. It had a peak ground acceleration (PGA) of 1.497g. The motion used from the 1971 San Fernando quake came from the Pacoima Dam station. It is located 2.8km from the fault rupture. The PGA was 1.226g. The motion used from the 1983 Coalinga quake came from the Pleasant Valley station, which is located 8.5km from the fault rupture. The PGA was 0.38g, but the entire record was scaled up to make the

PGA equal to 1g. The motion used from the 1999 Chi-Chi quake came from the WNT station. It is located 1.18km from the fault rupture. The PGA was 0.958g. However, the entire record was scaled to allow for a PGA of 2g.

## Analysis

### *Static Push-Over Analysis*

After applying the dead load to each system, a static push-over analysis was performed. The analysis was displacement controlled. It was found that the systems with conventionally detailed columns had identical push-over curves. The displacement capacity of RC and RCL was 17.76in (Fig. 7). The systems with unbonded post-tensioned columns also had push-over curves that were identical to one another. PT and PTL had displacement capacities of 12.81in. It was expected that the systems with unbonded post-tensioning would have smaller displacement capacities.

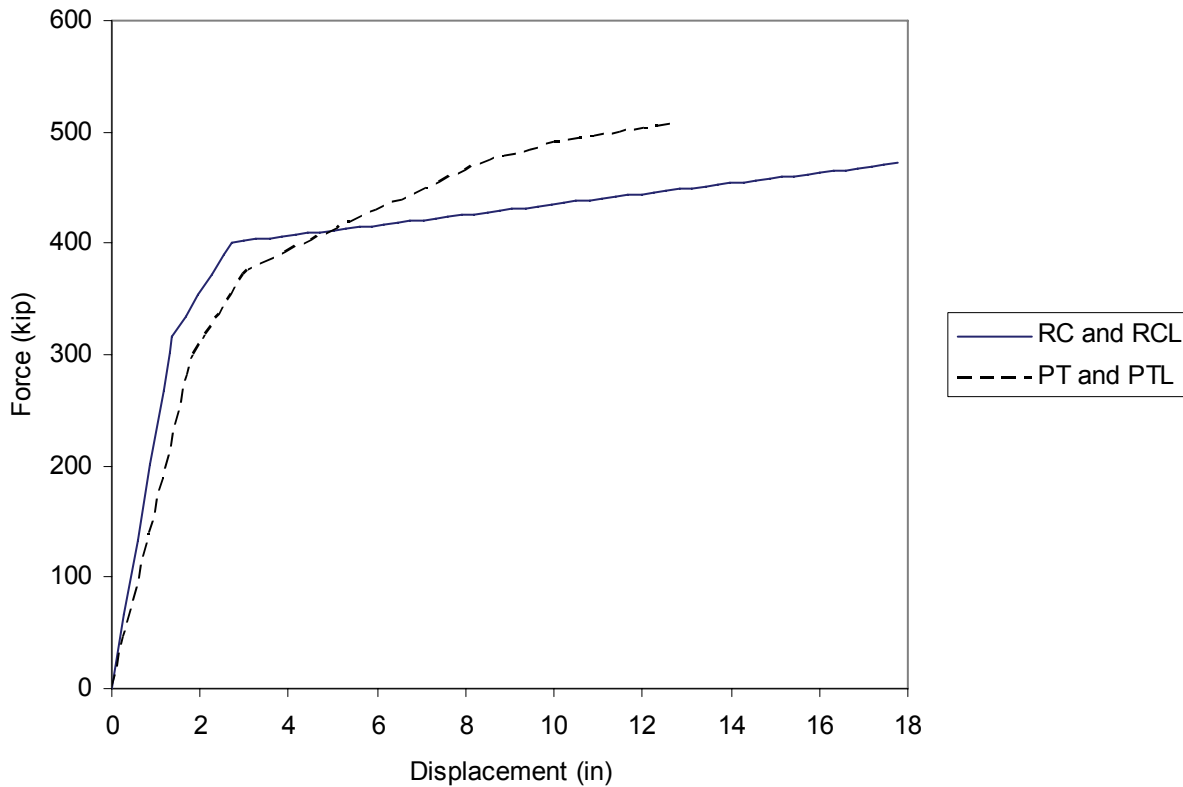


**Figure 7.** Static push-over curve

### *Cape Mendocino Earthquake Analysis*

From Table 2, it can be seen that the maximum displacement of PT was 0.39in larger than the maximum displacement of RC. As discussed earlier, this was expected, and it is a sign that the system with the post-tensioned column dissipated less energy. The systems with the

LRBs significantly contributed to decreasing peak displacements and thusly contributed to energy dissipation. RCL underwent 0.76in less displacement than RC, and PTL experienced 0.69in less displacement than PT.

The post-tensioning in the column significantly reduced the residual displacement. RC and PT had residual displacements of 4.08in and 2.39in, respectively, for a difference of 1.69in. Adding an LRB to the system with the conventionally detailed column slightly reduced residual displacement; the difference between RC and RCL was 0.24in. Adding LRBs to PT did not further decrease the residual displacement. The addition increased the residual displacement by 0.07in; however, this increase was considered negligible.

**Table 2.** Displacements from Cape Mendocino earthquake analysis

	RC	PT	RCL	PTL
Peak displacement (in)	9.70	10.09	8.94	9.40
Residual displacement (in)	4.08	2.39	3.84	2.46

*San Fernando Earthquake Analysis*

The maximum displacement of the RC system was 13.20in, which was 0.51in less than the PT system (Table 3). This was expected. It is worth noting that the 13.71in peak displacement experienced by PT was greater than its capacity. Therefore, the column failed. Again, the LRB systems reduced the maximum displacements. In this case, the PTL system was comparable to the RCL system. A significant finding is that adding LRBs to the post-tensioned column system reduced the peak displacement by 1.34in. For this particular earthquake, that addition was the difference between failure and survival of the structure.

Residual displacements for RC and RCL were 4.48 and 4.21in. The residual displacement of PT was 5.68in, which was greater than the residual displacement of RC. This was unexpected; however, the PT system exceeded its displacement capacity during analysis. Therefore, the column failed. For particularly strong earthquakes, the limited drift capacity of post-tensioned columns is a liability. This is related to what Billington and Kwan studied concerning survival and functional-level performance. The PTL system had a residual displacement of 2.11in. This result was over two inches better than any of systems with a conventionally designed column.

**Table 3.** Displacements from San Fernando earthquake analysis

	RC	PT	RCL	PTL
Peak displacement (in)	13.20	13.71	12.42	12.37
Residual displacement (in)	4.48	5.68	4.21	2.11

*Coalinga Earthquake Analysis*

Strangely, the peak displacement for PT was 0.32in less than the peak displacement of RC (Table 4). This was unexpected. It is possible that the spectra of this Coalinga ground motion had a period that was more similar to RC than PT. Adding LRBs to RC reduced maximum displacement by 1.02in, but it made no change for PT.

The difference in residual displacement between RC and PT was 1.38in. Adding LRBs to PT increased the residual displacement by 0.67in; however, this value was still 0.60in smaller than the best of RC and RCL.

**Table 4.** Displacements from Coalinga earthquake analysis

	RC	PT	RCL	PTL
Peak displacement (in)	11.54	11.12	10.52	11.12
Residual displacement (in)	3.13	1.75	3.02	2.42

*Chi-Chi, Taiwan Earthquake Analysis*

As expected, peak displacements were larger for the post-tensioned column systems than for their respective conventionally detailed column counterparts (Table 5). This is a sign that they dissipated less energy. Although PTL had a larger peak displacement than RCL, its maximum displacement was still 1.04in smaller than RC and 1.73in smaller than PT.

Residual displacements for RC and PT were 2.88 and 1.76in, making for a difference of 1.12in. Adding LRBs to RC appeared to reduce residual displacement by 0.49in, while adding LRBs to PT did not appreciably change the residual displacement.

**Table 5.** Displacements from Chi-Chi, Taiwan earthquake analysis

	RC	PT	RCL	PTL
Peak displacement (in)	10.51	11.20	8.72	9.47
Residual displacement (in)	2.88	1.76	2.39	1.73

*Comparison Between RC and PT*

In all four dynamic analyses except for the Coalinga motion, the peak displacement of the conventionally detailed column system was smaller than the peak displacement of the unbonded post-tensioned column system by an average of 0.53in (Table 6). It may be reasonably stated that unbonded post-tensioned columns experienced greater peak displacements when subjected to strong ground motions.

**Table 6.** Difference in peak displacement between RC and PT

	$\Delta_{PT} - \Delta_{RC}$ (in)
Cape Mendocino	0.39
San Fernando	0.51
Coalinga*	-0.42
Chi-Chi	0.69
Average	0.53

\*result not used in calculation of average

Residual displacements were found to be greater in the conventionally detailed column system by an average of 1.40in (Table 7). This result was expected. It may be said that the post-tensioned columns experienced smaller residual displacements after being subjected to seismic loads.

**Table 7.** Difference in residual displacement between RC and PT

	$\Delta_{RC} - \Delta_{PT}$ (in)
Cape Mendocino	1.69
San Fernando*	-1.20
Coalinga	1.38
Chi-Chi	1.12
Average	1.40

\*result not used in calculation of average because of column failure

*Effects of Lead Rubber Bearings*

From Table 8, it is demonstrated that adding lead rubber bearings at the abutments impacted the peak displacement of the conventionally detailed column bridge system. The RCL had an average of 1.11in less maximum displacement.

**Table 8.** Difference in peak displacement between RC and RCL

	$\Delta_{RC} - \Delta_{RCL}$ (in)
Cape Mendocino	0.76
San Fernando	0.78
Coalinga	1.02
Chi-Chi	1.79
Average	1.11

Table 9 demonstrates that adding lead rubber bearings at the abutments slightly reduced the residual displacements of the system.

**Table 9.** Difference in residual displacement between RC and RCL

	$\Delta_{RC} - \Delta_{RCL}$ (in)
Cape Mendocino	0.24
San Fernando	0.27
Coalinga	0.11
Chi-Chi	0.49
Average	0.28

On average, adding LRBs to the unbonded post-tensioned system reduced peak displacement by 1.25in (Table 12). However, for the Coalinga earthquake it had no effect, and the PT system failed during the San Fernando earthquake due to excessive column drift. More analysis cases are needed in order to confidently say that adding LRBs reduces maximum displacement, though it does appear that saying so is likely true.

**Table 12.** Difference in peak displacement between PT and PTL

	$\Delta_{PT} - \Delta_{PTL}$ (in)
Cape Mendocino	0.69
San Fernando	1.34
Coalinga	0
Chi-Chi	1.73
Average	1.25

There does not appear to be any correlation among the data concerning the addition of LRBs to the PT system (Table 13). In the Cape Mendocino and Chi-Chi analyses, residual displacements increased, though the values they increased by were negligible. There was a reduction in residual displacement during the Coalinga ground motion, but it is too difficult to draw any conclusions without further research.

**Table 13.** Difference in residual displacement between PT and PTL

	$\Delta_{PT} - \Delta_{PTL}$ (in)
Cape Mendocino	-0.07
San Fernando*	-3.57
Coalinga	0.67
Chi-Chi	-0.03
Average	0.19

\*result not used in calculation of average because of column failure

### Conclusion

A push-over analysis showed that a column with unbonded post-tensioning for the longitudinal reinforcement has a smaller displacement capacity than a column with mild steel reinforcement. Through a series of dynamic analyses, it was shown that the peak displacements of unbonded post-tensioned columns are greater than the peak displacements of a conventionally detailed column. This is a sign that the unbonded post-tensioned columns dissipate less energy. It was also shown that using unbonded post-tensioning instead of bonded reinforcing steel in a column reduces the residual displacements due to seismic loads. Adding lead rubber bearings at the abutment has the effect of reducing peak displacements for both systems. Use of both unbonded post-tensioning and lead rubber bearings may be a solution to the problems of residual displacement and energy dissipation, but further and more detailed research is needed.

It would be more beneficial to carry out an experimental study of the four proposed systems because it is very possible that the computer analysis did not provide accurate results. As mentioned earlier in this paper, Mahin et. al. found that the difference in residual displacements between their analysis and experiment was on the order of 100%.

If this analysis is to be repeated, the moment capacity of the column with unbonded post-tensioning should be closer to the moment capacity of the conventionally detailed column. As it stood, the moment capacities of RC and RCL were within 7.4% of the targeted capacity, and PT and PTL were within 0.1% of the targeted capacity. It is uncertain whether this impacted the results. Also, choosing a wider selection of ground motions would be beneficial. The reason for this would be to employ Billington and Kwan's definition of functional and survival-level

performance. These performance based designed criteria may provide better comparisons of the effectiveness of post-tensioning and lead rubber bearings.

### Acknowledgements

Great appreciation goes to the Network for Earthquake Engineering Simulation for sponsoring an enjoyable and educational summer. The idea for this research was given to the author by Dr. David Sanders. He provided valuable guidance and support at every stage of the study. Kevin Almer taught the author how to use SAP2000. He also provided numerous resources that aided in the calculations of stiffness values and development of the confined concrete model. Dr. Ian Buckle guided the author through the selection of the lead rubber bearing and the determination of its behavior. Special thanks go to Michael Taylor for helping develop and troubleshoot the analysis models as well as for providing invaluable advice. Lastly, this study would not have been possible without the previous work done by Ryo Yamashita. His thorough calculations and demonstrations were the foundation for modeling the unbonded post-tensioned systems.

### References

- Almer, K., and Sanders, D. "Precast Beams with Cast-In-Place Connections." Proceedings of the 22<sup>nd</sup> US-Japan Bridge Engineering Workshop, Seattle, WA, October 23-25, 2006. 262-274.
- Buckle, I.G., and Mayes, R.L. "Seismic Retrofit of Bridges using Mechanical Energy Dissipators." Proceedings of Fourth US National Conference on Earthquake Engineering, Palm Springs, California, May 20-24, 1990. Vol. 3, 305-314.
- Kwan, W.-P., and Billington, S. L. "Unbonded Post-tensioned Concrete Bridge Piers. I: Monotonic and Cyclic Analyses." *Journal of Bridge Engineering*, Vol. 8, No. 2, March 1, 2003, 92-101.
- Kwan, W.-P., and Billington, S. L. "Unbonded Post-tensioned Concrete Bridge Piers. II: Seismic Analyses." *Journal of Bridge Engineering*, Vol. 8, No. 2, March 1, 2003, 102-111.
- Mahin, S., Sakai, J., and Jeong, H. "Use of Partially Prestressed Reinforced Concrete Columns to Reduce Post-Earthquake Residual Displacements of Bridges." Fifth National Seismic Conference on Bridges & Highways, San Francisco, California, September 18-20, 2006. Paper No. B25.
- Mander, J.B., Priestley, M.J.N., and Park, R. "Theoretical Stress-Strain Model for Confined Concrete." *Journal of Structural Engineering*, Vol. 114, No. 8, August, 1988, 1804-1812.
- Yamashita, R., and Sanders, D. "Shake Table Testing and an Analytical Study of Unbonded Prestressed Hollow Concrete Columns Constructed with Precast Segments." A Report for PC Bridge Co., Ltd., Tokyo, Japan, August 2005. Report No. CCEER 05-9.

### Appendix

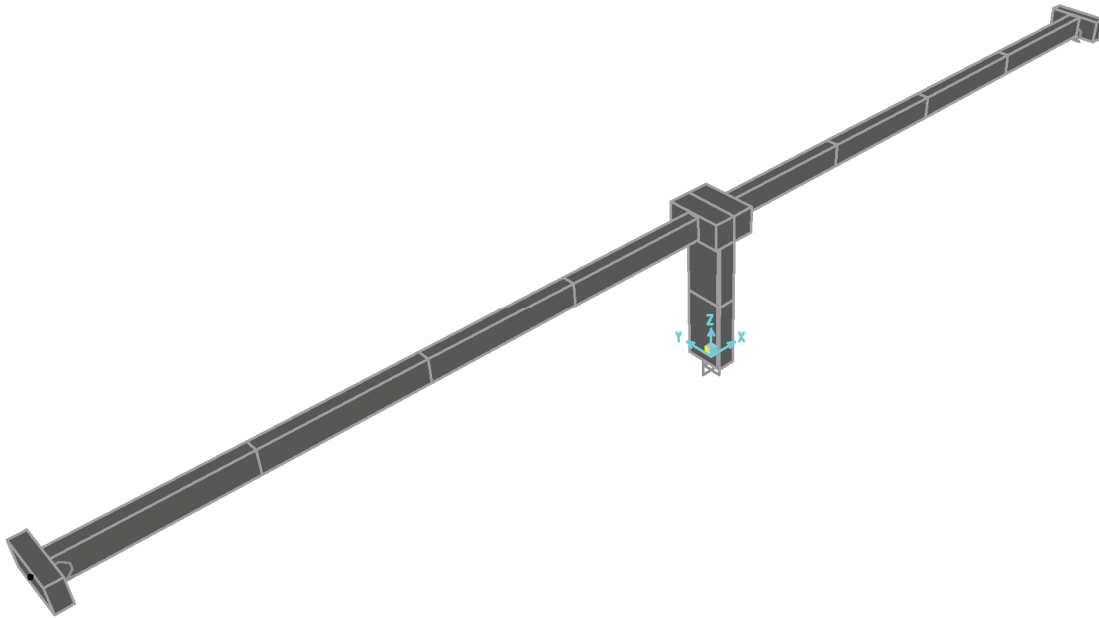


**Figure 8.** 3-D view of SAP2000 analysis template

### *Mander's Confined Concrete Model*

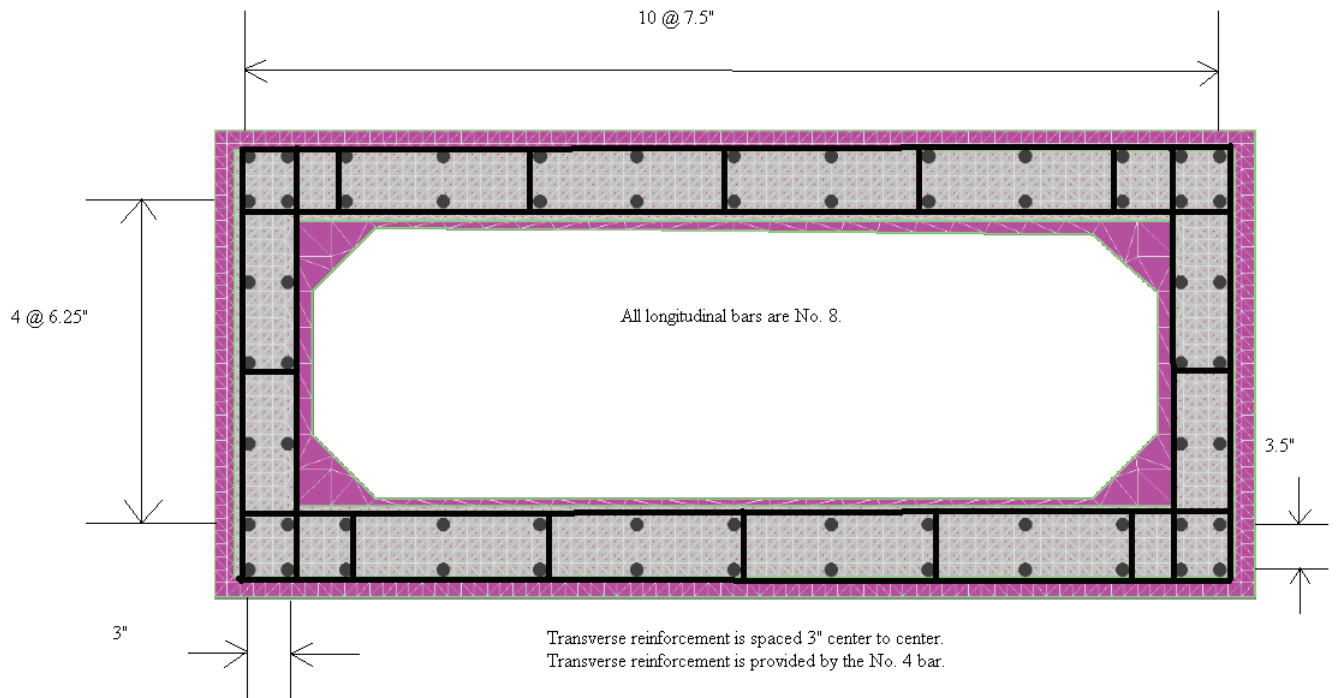


**Figure 9.** Reinforcement details for RC

The following steps detail the calculations used to define the confined concrete model. First, a cross-section was designed (Fig. 9). The ratios of the confining steel in the x and y-directions were calculated using Eqs. 1 and 2. Then, the lateral confining stress ratios were calculated in the x and y-directions using Eqs. 3 and 4. The ratios of lateral confining stress to unconfined concrete strength were found in the x and y-directions. These ratios determined the confined concrete strength ratio via Fig. 4 from “Theoretical Stress-Strain Model for Confined Concrete” (Mander et. al., 1988). Once the confined concrete strength ratio was found, Eq. 5 was used to determine the strength of the confined concrete. The last value found was the crushing strain (Eq. 6). In order to calculate the crushing strain of the confined concrete, it was assumed that the crushing strain of the unconfined concrete was 0.002. Variables, definitions, and values used in the calculations are shown in Table 14. Determining the confined concrete strength and crushing strain was necessary to perform a moment-curvature analysis in XTRACT.

$$\rho_y = \frac{A_{sy}}{s * b_c} \tag{Eq. 1}$$

$$\rho_x = \frac{A_{sx}}{s * d_c} \tag{Eq. 2}$$

$$f_{lx} = 0.75 * \rho_x * f_{yh} \tag{Eq. 3}$$

$$f_{ly} = 0.75 * \rho_y * f_{yh} \tag{Eq. 4}$$

$$f_{cc} = K * f_c \tag{Eq. 5}$$

$$\epsilon_{cc} = \epsilon_c \left( 1 + 5 * \left( \frac{f_{cc}}{f_c} - 1 \right) \right) \tag{Eq. 6}$$

**Table 14.** Mander’s confined concrete model

s	center to center spacing between transverse reinforcement	3"
d <sub>c</sub>	core dimension to centerline of hoop in x direction	75"
b <sub>c</sub>	core dimension to centerline of hoop in y direction	32"
A <sub>sx</sub>	area transverse steel in x direction	1sq in
A <sub>sy</sub>	area of transverse steel in y direction	1.8sq in
ρ <sub>x</sub>	steel to concrete ratio in x	0.01042
ρ <sub>y</sub>	steel to concrete ratio in y	0.008
f <sub>lx</sub>	lateral confining stress in x direction	0.5314ksi
f <sub>ly</sub>	lateral confining stress in y direction	0.408ksi
f <sub>c</sub>	28-day strength of concrete	5ksi
f <sub>yh</sub>	yield stress of transverse reinforcement	68ksi
K	confined strength ratio	1.5
f <sub>cc</sub>	strength of confined concrete	7.5ksi
ε <sub>c</sub>	crushing strain of unconfined concrete	0.002
ε <sub>cc</sub>	crushing strength of confined concrete	0.007

*Moment-Rotation Relationship for RC*

The following steps detail the calculations used to determine the moment-rotation relationship. First, an XTRACT moment-curvature analysis provided critical information (Table 15). Then, the rotation that occurs between yielding and failure was determined using Eq. 7. The effective yield and ultimate rotations were calculated with Eqs. 8 and 9. XTRACT provided the effective yield and ultimate moments. With this information, the moment-rotation relationship was defined (Fig. 4). The axial and shear stiffness were calculated using Eqs. 10 and 11. These stiffness values were treated as linear in SAP2000.

$$\theta_p = L_p (\phi_u - \phi_y) \tag{Eq. 7}$$

$$\theta_y = \frac{M_y}{EI} \frac{L}{L} \tag{Eq. 8}$$

$$\theta_u = \theta_y + \theta_p \tag{Eq. 9}$$

$$u_1 = \frac{E * A}{L} \tag{Eq. 10}$$

$$u_2 = \frac{12EI}{L} \tag{Eq. 11}$$

**Table 15.** Definition of link element of RC

A	area	1570.625
L	plastic hinge length in SAP2000	0.1
E	modulus of elasticity of concrete	4031
EI	effective EI at yield	7256000
L <sub>p</sub>	length of plastic hinge	36
φ <sub>y</sub>	effective yield curvature	8.70E-05
φ <sub>u</sub>	ultimate curvature	1.69E-03
M <sub>y</sub>	effective yield moment	57470
M <sub>u</sub>	ultimate moment	69130
θ <sub>p</sub>	rotation between yielding and failure	5.78E-02
θ <sub>y</sub>	yield rotation	7.92E-04
θ <sub>u</sub>	ultimate rotation	5.86E-02
u <sub>1</sub>	axial stiffness	63311894
u <sub>2</sub>	major shear stiffness	87072000000

units in kilo pound, inch, and radian

### *Moment-Drift Relationship*

The flexural design of the post-tensioned column was completed first. This was an iterative process. The axial load at the base of the column was determined from a SAP2000 dead load analysis. Then strand sizes and properties were selected. The strands had an ultimate strength of 270ksi. The area of a single strand was 0.153sq in. An effective pre-stress of 0.60 was assumed. Yamashita used double the length of his column as his effective length in calculations. Since the column studied here was in double curvature, the effective length was assumed to be equal to the length of the column. The stress in each group of steel strands was calculated using Eq. 12. The initial depth of the neutral axis,  $c$ , was assumed. Next, the tension force in each group of strands was calculated. The length of the equivalent stress block was calculated using Eq. 13. According to ACI code, the length of the equivalent stress block,  $c$ , is equal to a factor times  $a$ . The factor varies depending on the compressive strength of the concrete. For 5ksi concrete, 0.80 is the factor. Once a value was determined for  $a$ , the value of  $c$  was updated, and the process was repeated until it converged. With the depth of the neutral axis known, the compressive concrete force was calculated using Eq. 14. The moment due to each pre-stressing strand was calculated by multiplying the force in each strand by its effective depth, and the moment due to the concrete compressive force was calculated using Eq. 15. The summation of the moments is the moment capacity of the column. For a list of variables, values, and definitions, see Table 16.

$$f_{ps-i} = f_{pe} + 900 \left( \frac{d_i - c}{L_e} \right) \leq f_{pu} \quad (\text{Eq. 12})$$

$$a = \frac{T + P}{0.85 * f'_c * b} \quad (\text{Eq. 13})$$

$$C = 0.85 * f'_c * a * b \quad (\text{Eq. 14})$$

$$M_c = C \left( c - \frac{a}{2} \right) \quad (\text{Eq. 15})$$

**Table 16.** Flexural design of post-tensioned column

		tension flange	web	compression flange	corners of t. flange	corners of c. flange
P	axial force at base	445.73				
$f_{pu}$	ultimate strength	270				
$f_{pe}$	effective stress	162				
n	number of strands	11	11	11	9	9
N	number of strand locations	3	2	3	2	2
$d_i$	effective depth	32.25	18	3.75	32.25	3.75
$A_{ps}$	total area of strands	5.049	3.366	5.049	2.754	2.754
$L_e$	effective length	313.75				
c	neutral axis depth	4.14				
$f_{ps-i}$	stress in each steel strand	242.62	201.74	160.87	242.62	160.87
$T_i$	tension force	1224.99	679.07	812.22	668.18	443.03
a	equivalent stress block	6.25				
C	compression force	4273.23				
$M_c$	moment due to C	140472.05				
$M_T$	moment due $T_i$	39506.05	12223.30	3045.84	21548.76	1661.37
$M_n$	nominal moment	218457.36				
$\phi_f$	reduction factor	0.79				
$\phi_f M_n$	capacity	172581.32				

units in kilo pound and inch

After flexural design, the drift and moment and joint opening were determined. First, the moment at joint opening was calculated using Eq. 16. Then, the displacement at the joint due to flexure was calculated using Eq. 17. The length of the column was assumed to be half of the actual length since the column studied was in double curvature. The lateral shear force and lateral shear stiffness were calculated using Eqs. 18 and 19. The displacement of the joint due to shear was calculated using Eq. 20. Lastly, the drift at joint opening was found by adding the displacements and dividing by the column length. The variables, definitions, and values used for these calculations are shown in Table 17.

$$M_o = \sigma_i * \frac{I}{y} \tag{Eq. 16}$$

$$\delta_{of} = \frac{P_o * l_c^3}{3 * E_c * I} \tag{Eq. 17}$$

$$P_o = \frac{M_o}{L_c} \tag{Eq. 18}$$

$$K_s = \frac{E_c * b_w * d}{3 * l_c} \tag{Eq. 19}$$

$$\delta_{of} = \frac{P_o}{K_s} \tag{Eq. 20}$$

**Table 17.** Moment and drift at joint opening

$\sigma_i$	initial compressive stress	2.24
$I$	moment of inertia of gross column section	266016
$y$	half of section depth	18
$M_o$	moment at joint opening	33113.57
$P_o$	lateral force at joint opening	228.57
$l_c$	column height	144.88
$E_c$	modulus of elasticity of concrete	4031
$\Delta_{of}$	disp. at joint opening due to flexure	2.16E-01
$b_w$	total web width	15
$d$	effective depth of pre-stressing steel	32.25
$K_s$	shear stiffness for un-cracked section	4486.62
$\Delta_{os}$	disp. at joint opening due to shear	5.09E-02
$x_o$	drift at joint opening	1.84E-03

units in kilo pound and inch

The moments and drifts of the pre-stressing steel at yielding and failure were found by using Eq. 21. This equation was proposed and validated through experimentation by Yamashita. The initial strain in the pre-stressing steel and the strain in the pre-stressing steel at yielding were assumed from code specifications. The strain in the pre-stressing steel at failure was determined by Yamashita through a series of tests on a single pre-stressing strand. In Yamashita's calculations, the length of the pre-stressing steel was the column length plus the height of his footing. Since the column studied here is rigid at both ends rather than cantilever, an average is taken between the height of the integral connection and the column footing. An average of four feet was used, and this was added to half of the column height. Therefore, the length of the pre-stressing steel was 192.88in. Variables, definitions, and values for the determination of the drift at yielding and failure are shown in Table 18.

$$\epsilon_{ps} = \epsilon_{pe} + 1050000 \left( \frac{d_i - t_f}{l_p} \right) x \quad (\text{Eq. 21})$$

**Table 18.** Moment and drift of pre-stressing steel at yield and failure

$x_{rm}$	max. location of resultant compression force	14.25
$e_{pe}$	initial strain in pre-stressing steel	5680
$e_{ps-y}$	strain in pre-stressing steel at yielding	8600
$e_{ps-f}$	strain in pre-stressing steel at failure	10500
$d_t$	depth of pre-stressing steel in tension flange	32.25
$t_f$	thickness of compression flange	7.5
$l_p$	length of pre-stressing steel	192.88
$x_y$	drift at yielding	2.17E-02
$x_f$	drift at failure	3.58E-02

units in kilo pound and inch

The resultant location of the compression force at joint opening was found. The strains in the different strand locations were found using Eq. 21. From these strains, the stress in each group of strands was found using Eq. 22. Next, the tensile force in each group of strands was calculated. Using Eq. 23, the compressive force was calculated. Lastly, the moment at joint opening was calculated using Eq. 24. Variables, definitions, and values are shown in Table 19.

$$\sigma_{ps} = 28500 * \epsilon_{ps} \text{ for } \epsilon_{ps} \leq 8600 \quad (\text{Eq. 22})$$

$$C = T + P \quad (\text{Eq. 23})$$

$$M = C * x_r + T_t(d_t - y) + T_c(d_c - y) \quad (\text{Eq. 24})$$

**Table 19.** Calculation of the resultant location of the compressive force

$M_o$	theoretical moment at joint opening	33113.57
$x_o$	theoretical drift at joint opening	1.84E-03
$\epsilon_{pe}$	initial strain in pre-stressing steel	5680
$d_t$	depth of pre-stressing steel in tension flange	32.25
$d_w$	depth of pre-stressing steel in web	18
$d_c$	depth of pre-stressing steel in compression flange	3.75
$t_f$	thickness of compression flange	7.50
$l_p$	length of pre-stressing steel	192.88
$\epsilon_{ps-ot}$	strain in pre-stressing steel in tension flange	5928.31
$\epsilon_{ps-ow}$	strain in pre-stressing steel in web	5785.34
$\epsilon_{ps-oc}$	strain in pre-stressing steel in compression flange	5642.38
$\sigma_{ps-ot}$	stress in pre-stressing steel in tension flange	168.96
$\sigma_{ps-ow}$	stress in pre-stressing steel in web	164.88
$\sigma_{ps-oc}$	stress in pre-stressing steel in compression flange	160.81
$A_{ps-t}$	area of pre-stressing steel in tension flange	7.80
$A_{ps-w}$	area of pre-stressing steel in web	3.37
$A_{ps-c}$	area of pre-stressing steel in compression flange	7.80
$T_t$	tensile force in tension flange	1318.37
$T_w$	tensile force in web	554.99
$T_c$	tensile force in compression flange	1254.78
$T_{total}$	total tensile force	3128.15
$P$	axial force at base of column	445.73
$C$	compression force	3573.88
$y$	half of section depth	18
$x_{ro}$	resultant location at joint opening	9.01

units in kilo pound and inch

It was assumed that the relationship between the resultant location of the compression force and the drift was linear until the resultant location of the compression reached its maximum value, which was assumed to be at the center of the compression flange. The point at which the resultant location of the compression force achieved its maximum value was defined as B. With the drifts known at joint opening, yielding, and failure, the only unknown drift was at B. This was calculated using Eq. 25. The strain in each group of strands was calculated using Eq. 21. Depending on the strain value, stress in each group of strands was calculated using either Eq. 22 or Eq. 26. Lastly, the moments at B, yielding, and failure were calculated using Eq. 24. Variables, definitions, and values used in the calculation process are shown in Table 20. The moment-drift relationship is displayed in Fig. 10.

$$\frac{x_o}{x_{ro}} = \frac{x_b}{x_{rm}} \tag{Eq. 25}$$

$$\sigma_{ps} = 270 - \left( \frac{0.04}{\epsilon_{ps} - 0.007} \right) \text{ for } \epsilon_{ps} \geq 8600 \tag{Eq. 26}$$

**Table 20.** Calculation of the moment at B, yielding, and failure

		B	Yielding	Failure
x	drift	2.91E-03	2.17E-02	3.58E-02
$\epsilon_{ps-t}$	strain in pre-stressing steel in tension flange	6072.64	8600	10500
$\epsilon_{ps-w}$	strain in pre-stressing steel in web	5846.57	6918.79	7724.85
$\epsilon_{ps-c}$	strain in pre-stressing steel in compression flange	5620.51	5237.58	4949.70
$\sigma_{ps-t}$	stress in pre-stressing steel in tension flange	173.07	245.00	258.57
$\sigma_{ps-w}$	stress in pre-stressing steel in web	166.63	197.19	220.16
$\sigma_{ps-c}$	stress in pre-stressing steel in compression flange	160.18	149.27	141.07
$T_t$	tensile force in tension flange	1350.47	1911.74	2017.63
$T_w$	tensile force in web	560.87	663.73	741.05
$T_c$	tensile force in compression flange	1249.92	1164.76	1100.74
$T_{total}$	total tensile force	3161.25	3740.22	3859.43
N	axial force at base of column	445.73		
C	compression force	3606.98	4185.95	4305.16
M	moment at base	52832	70294	74414

units in kilo pound and inch

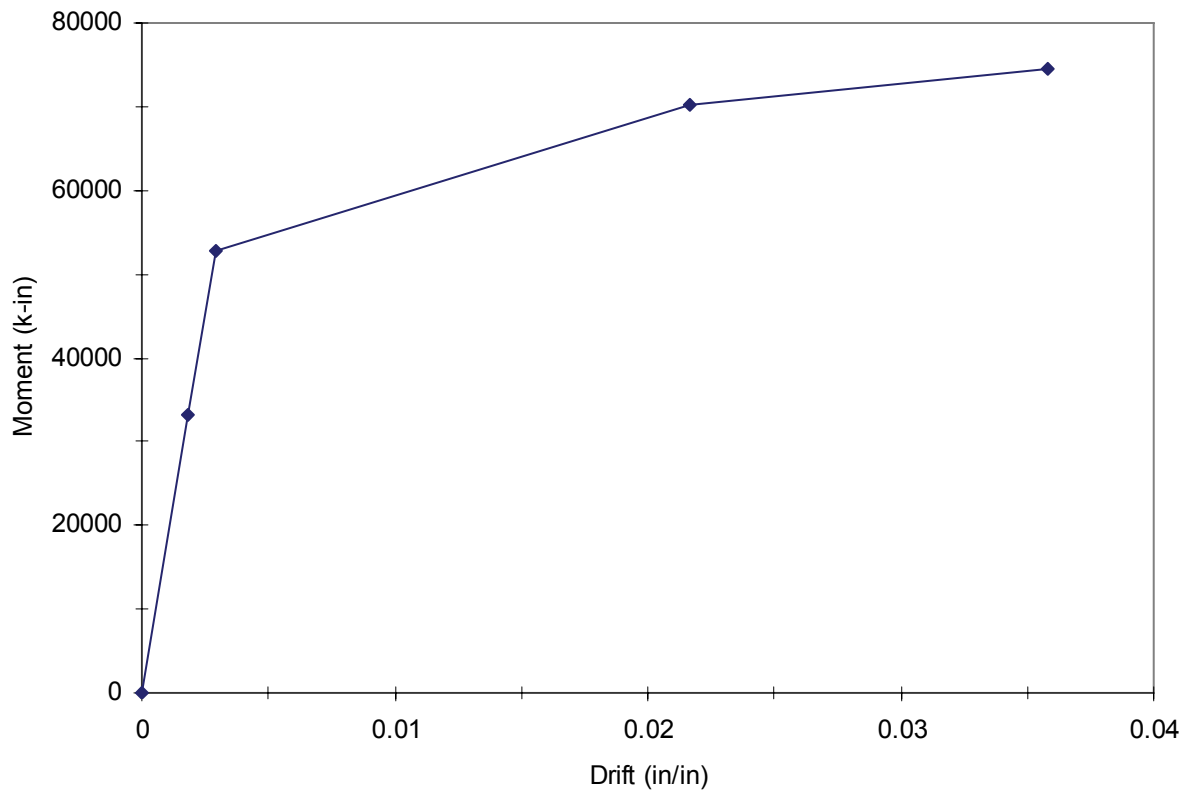


**Figure 10.** Moment-drift relationship for PT

*Plastic Hinge Properties for PT*

The rotation of the column at a given drift was found by taking the arctangent of the drift. Since the values of drift are very small, the drift was approximately equal to the rotation. The moment-rotation relationship is shown in Table 21 and Fig. 6. Axial stiffness was calculated using Eq. 10. Shear stiffness was calculated using Eqs. 8 and 11. Stiffness values are shown in Table 22.

**Table 21.** Moment-rotation relationship for PT

	Joint Opening	B	Yielding	Failure
M	33114	52832	70294	74414
$\theta$	1.84E-03	2.91E-03	2.17E-02	3.58E-02

units in kilo pound, inch, and radian

**Table 22.** Axial and shear stiffness for PT

A	gross column area	1570.63
$M_y$	yield moment	70294
L	length of plastic hinge in SAP2000	0.1
EI	effective EI at yield	3.24E+06
$u_1$	axial stiffness	6.33E+07
$u_2$	major shear stiffness	3.89E+10

units in kilo pound and inch

*Lead Rubber Bearings*

The lead rubber bearings were designed from information provided by the Dynamic Isolation Systems, Inc. website. From a dead load analysis, it was determined that the reaction at each abutment was less than 90kip. A 12in diameter isolator with an axial load capacity of 100kip was selected for use in the model. The isolator was modeled as a link element. Multi-linear plastic was chosen for the type of link. Axial deformation and rotation were restricted. It was necessary to define a hysteresis for the isolator in order to model the nonlinear behavior. A linear relationship was assumed from initial stiffness to yielding and from yielding to failure. Eq. 27 was used to find the initial stiffness of the lead rubber bearing. The deformation at yielding was calculated with Eq. 28. Yield strength was found from Eq. 29, and maximum strength was found with Eq. 30. Variables, definitions, and values are shown in Table 23. See Fig. 11 for the hysteresis.

$$K_e = 10 * K_d \tag{Eq. 27}$$

$$\Delta_y = \frac{Q_d}{K_e - K_d} \tag{Eq. 28}$$

$$F_y = K_e \Delta_y \tag{Eq. 29}$$

$$F_{max} = Q_d + K_d (\Delta_{max} - \Delta_y) \tag{Eq. 30}$$

**Table 23.** Lead rubber bearing properties

D	isolator diameter	12"
K <sub>d</sub>	yield stiffness	5kip/in
Q <sub>d</sub>	characteristic strength	15kip
K <sub>e</sub>	initial stiffness	50kip/in
Δ <sub>max</sub>	maximum displacement	6"
Δ <sub>y</sub>	yield displacement	0.33"
F <sub>y</sub>	yield strength	16.67kip
F <sub>max</sub>	maximum strength	43.33kip

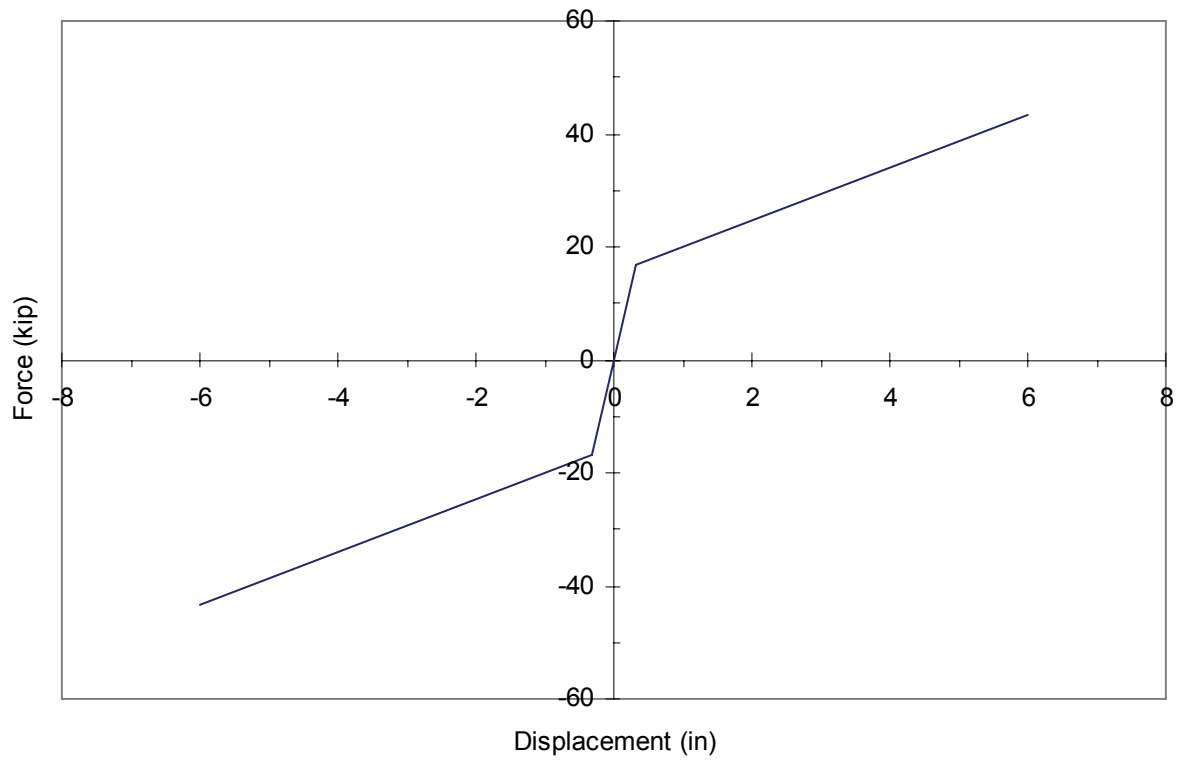


**Figure 11.** LRB hysteresis